



Deployment kinematics of axisymmetric Miura origami: Unit cells, tessellations, and stacked metamaterials

Xiangxin Dang ^a, Lu Lu ^a, Huiling Duan ^{a,b}, Jianxiang Wang ^{a,b,*}

^a State Key Laboratory for Turbulence and Complex Systems, Department of Mechanics and Engineering Science, College of Engineering, Peking University, Beijing 100871, China

^b CAPT-HEDPS, and IFSA Collaborative Innovation Center of MoE, College of Engineering, Peking University, Beijing 100871, China



ARTICLE INFO

Keywords:

Axisymmetric Miura origami
Deployment kinematics
Locking mechanism
Stacked metamaterials

ABSTRACT

Origami is emerging as a promising paradigm for deployable structures. The theoretical analysis on the relationship between geometry of the crease patterns and the induced deployment mechanisms is the key to the rational design of origami-inspired deployable structures. In this paper, we systematically investigate the deployment kinematics of axisymmetric Miura origami from unit cells to single-layer tessellations and multi-layer stacked metamaterials. We show that the axisymmetric Miura cells can be classified into two categories according to the monotonicity of the angular motion, and the axisymmetric Miura origami tessellations can be classified into seven categories based on the developability, flat-deployability, and the ability to form closed-ring shapes. We also derive the conditions for the deployability of the multi-layer metamaterials constructed by stacking axisymmetric Miura origami tessellations. Both the singly and doubly curved cases are studied for the tessellations and metamaterials. Additionally, based on the kinematic formulations, we develop an easy-to-implement optimization framework for the design of doubly curved axisymmetric Miura origami tessellations that approximate surfaces of revolution. The optimized shape-morphing tessellations can also be used to assemble multi-layer stacked metamaterials. Taken together, these results provide a comprehensive guidance to design axisymmetric deployable structures based on origami principles.

1. Introduction

Axisymmetry, also known as rotational symmetry, is one of the most common types of symmetry in geometry. Many natural objects exhibit axisymmetric morphology such as sympetalous flowers [1] and pendant drops [2]. Also, artificial axisymmetric shell structures, benefiting from the favorable thermal performance and high strength-to-weight ratio, are extensively applied in engineering to build domed roofs [3], hyperbolic cooling towers [4], storage silos [5], etc. In space engineering, deployable axisymmetric structures have gained great importance for the design of telescopes and space antennas [6–8]. Deployability enables the large space devices to be packaged compactly in spacecraft and spread after launched into the orbit. In addition to astronautics, nowadays, deployable axisymmetric structures can be found in diverse fields such as architecture [9], soft robotics [10], materials science [11], and medical science [12].

Origami is an ancient art of folding paper, dating back to more than one thousand years ago [13]. For recent decades, mathematical rules have been developed to guide the design of origami [14–16],

promoting it beyond an art form to a scientific technique that can shift two dimensional (2D) sheets to three dimensional (3D) structures [17]. Specifically, the rational understanding of the relations between crease patterns and the induced foldability is critical to the precise control of the folding path of origami-inspired structures [18–36]. Meanwhile, origami technique is emerging as a new paradigm of deployable typologies [8], and finds various applications including deployable arrays [37,38], reconfigurable metamaterials [39,40], origami robots [41–43], shape-morphing tessellations [44–49], and micro-/nano-electromechanical systems [50]. Besides, origami-inspired structures can possess distinctive mechanical responses such as negative Poisson's ratio [51–53], graded stiffness [54,55], multistability [56–59], and high energy absorption efficiency [60,61]. And more importantly, the variation of crease patterns allows a tunable and programmable design of these mechanical properties [62–69].

Classical origami patterns are generally composed of repeated polygonal cells. Typical examples include the Miura-ori pattern [37], Kresling pattern [70], square-twist pattern [71], Resch's pattern [72],

* Corresponding author at: State Key Laboratory for Turbulence and Complex Systems, Department of Mechanics and Engineering Science, College of Engineering, Peking University, Beijing 100871, China.

E-mail address: jxwang@pku.edu.cn (J. Wang).

and waterbomb pattern [73]. Among these, Miura-ori pattern is tessellated by congruent parallelograms, which can be treated as a floppy mechanism with a single degree of freedom. This feature of motion greatly benefits applications in request of controlled folding or deployment. As a result, Miura origami has been attracting considerable attention in engineering and the scientific community since it was first invented as a solution of the packaging and deployment for large spatial membranes by the Japanese astrophysicist Koryo Miura in 1985 [37]. Subsequently, the celebrated Miura-ori was found to be embedded in a much larger space of quadrilateral-mesh folding systems provided with developability, rigid-foldability, as well as the single degree of freedom [20]. The latter is now thoroughly characterized as the rigidly and flat-foldable quadrilateral mesh origami (RFFQM) [33]. Various modified Miura-ori patterns that are contained in the RFFQM have been specially investigated, such as the cylindrical pattern [27, 29, 45, 47], the axisymmetric pattern [23, 46, 47], and the isomorphic/non-isomorphic symmetric patterns [25, 26]. In particular, the axisymmetric pattern is constructed with tapered Miura-ori strips that are replicated in the circumferential direction, and therefore can be deployed into annular shapes with rotational symmetry. In this work, we refer to this category of RFFQM as the *axisymmetric Miura origami* (AMO), which is a promising candidate for deployable axisymmetric structures.

Current studies of AMO are mainly focused on the shape morphing for surfaces of revolution. Gattas et al. [23] gave an original example of AMO forming a conical shape in their work on the Miura-derivative origami patterns. Song et al. [46] used AMO to design flat-deployable and flat-foldable origami structures that can be deployed into closed-ring shapes that approximate various surfaces of revolution with positive and negative Gaussian curvatures. Hu et al. [47] reported that a shape-morphing AMO structure can get locked at two isolated annular configurations if there are plenty of Miura-ori strips replicated in the circumferential direction. Under this circumstance, the AMO structure is flat-foldable at one annular configuration and flat-deployable at the other, but cannot transform from one to the other through rigid deployment. By contrast, if the number of replicated Miura-ori strips is relatively small, the AMO structure will keep non-closed shapes on the entire deployment path between the folded-flat and deployed-flat configurations. Despite various examples of the shape-morphing AMO structures given in [23, 46, 47], the relationship between the axisymmetric crease patterns and the induced deployment mechanisms is not fully explored. In this regard, some key questions are yet to be answered: What geometric constraints of the crease distributions should be satisfied to build an AMO structure that can form a closed-ring shape upon deployment? How can one judge a crease pattern to be flat-foldable and flat-deployable, or corresponding to two isolated annular configurations? How can one build deployable multi-layer metamaterials by stacking various AMO tessellations? Answering these questions will give a comprehensive understanding of the design space of AMO, and therefore benefit the applications of AMO for axisymmetric deployable structures.

In this paper, we investigate the deployment kinematics of axisymmetric Miura origami at the levels of unit cells, single-layer tessellations, and multi-layer stacked metamaterials. The origami panels are assumed to be undeformable and have zero thickness, so that the deployment is achieved by the relative rotation of adjacent panels around the idealized hinges at the creases. Firstly, the deploying motion of the AMO cells is formulated in terms of the geometric and kinematic parameters. Secondly, the angular motion of the AMO tessellations is theoretically analyzed for different numbers of unit cells replicated in the circumferential direction. We will classify all the possible patterns of AMO tessellations into seven categories based on the developability, flat-deployability, and the ability to form closed-ring shapes. We also find that the angular motion of an AMO tessellation is independent of its radial geometry, the latter of which can be modified to change the out-of-plane deformation of the folded tessellation. This decoupling

effect inspires us to develop a simple and effective optimization framework for the shape-morphing design of AMO tessellations with fixed angular deployment behaviors. Finally, we construct the 3D metamaterials composed of stacked AMO tessellations of planar or non-planar folded shapes. The constraints on the geometry and deploying motion between adjacent AMO tessellations are presented.

2. Unit cell kinematics

The unit cell of classical Miura origami has a degree-4 vertex and four congruent parallelograms [37]. The AMO cell, instead, has a degree-4 vertex at the joint of four trapezoids, as shown in Fig. 1(a). The geometry of the flat AMO cell is determined by the side lengths a (the *circumferential edge length*), b (the *radial edge length*), and sector angles α (the *major sector angle*), β (the *minor sector angle*) with the constraint

$$0 < \beta < \alpha < \pi/2. \quad (1)$$

We define the *deviation length* d as the difference between the lengths of the edges P_2Q_2 and P_0Q_0 , i.e.,

$$d = \|\overline{P_2Q_2}\| - \|\overline{P_0Q_0}\|. \quad (2)$$

We denote the difference between the major sector angle and the minor sector angle by

$$\delta = \alpha - \beta, \quad (3)$$

and call δ the *deviation angle*. Using trigonometry, we have

$$2b \sin \delta = d \sin \beta. \quad (4)$$

The deviation angle δ or deviation length d characterizes the discrepancy of an AMO cell away from a Miura cell. Specifically, the trapezoids with $\delta = 0$ or $d = 0$ become parallelograms, and the AMO cell degenerates into the Miura cell under such circumstance. The folded AMO cell is demonstrated in Fig. 1(b). Similar to the Miura cell, the degree-4 vertex of the AMO cell has single degree-of-freedom motion that can be determined by the dihedral angles γ or φ . The relationship between γ and φ is given by [33]

$$\cos \gamma = \frac{(1 + \cos^2 \alpha) \cos \varphi + \sin^2 \alpha}{1 + \cos^2 \alpha + \sin^2 \alpha \cos \varphi}. \quad (5)$$

Interestingly, the vertically projected pattern of the folded AMO cell also consists of four trapezoids with axial symmetry, as shown in Fig. 1(c). Thus, the geometry of the projected pattern can be described by the *projected major sector angle* α' , the *projected minor sector angle* β' , the *projected circumferential edge length* a' , and the *projected radial edge length* b' . The *projected deviation length* d' and the *projected deviation angle* δ' can also be defined accordingly, which satisfy the following relationships:

$$d' = \|\overline{P'_2Q'_2}\| - \|\overline{P'_0Q'_0}\|, \quad (6)$$

$$\delta' = \alpha' - \beta', \quad (7)$$

$$2b' \sin \delta' = d' \sin \beta'. \quad (8)$$

The projected major sector angle α' is dependent on the dihedral angle φ following the spherical cosine rule [47]:

$$\cos 2\alpha' = \cos^2 \alpha + \sin^2 \alpha \cos \varphi. \quad (9)$$

Combining Eqs. (5) and (9), we can further obtain the relationship between α' and γ :

$$\sin \frac{\gamma}{2} = \frac{\tan \alpha'}{\tan \alpha}. \quad (10)$$

Eq. (10) indicates that the major projected angle α' varies monotonically with the dihedral angle γ , so that α' can be regarded as a

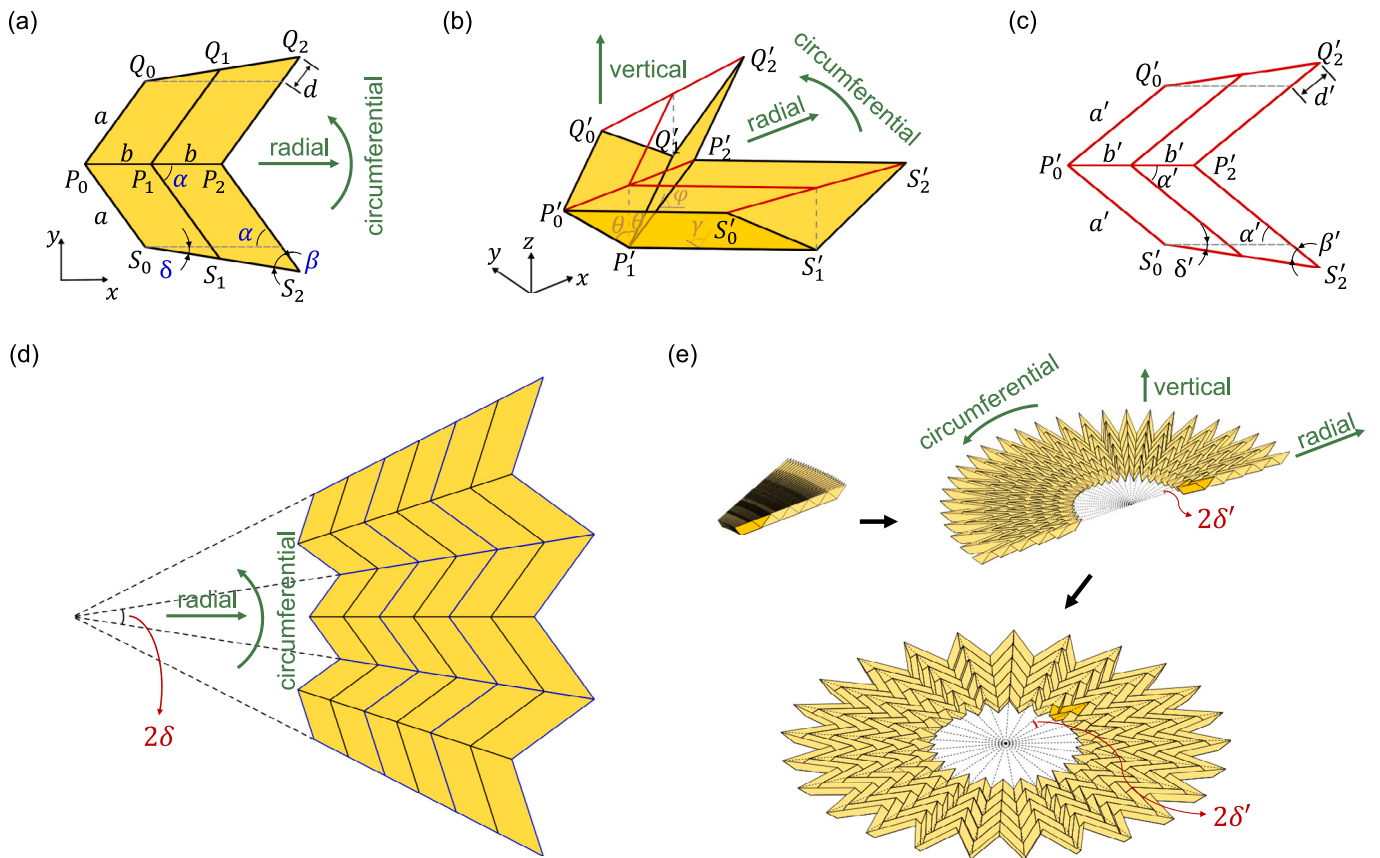


Fig. 1. Axisymmetric Miura origami. (a) The deployed-flat configuration of an AMO cell. (b) A folded configuration of the AMO cell. (c) The vertical projection of the folded unit cell. (d) The AMO tessellations are constructed by arranging AMO cells in the circumferential and radial directions. (e) An AMO tessellation composed of 25×5 unit cells. The tessellation can be deployed with a single degree of freedom from a compact folded state (top left, $2\delta' = 0.005\pi$) to a partially folded state (top right, $2\delta' = 0.04\pi$), and eventually form an closed-ring shape (bottom, $2\delta' = 0.08\pi$).

parameter that traces the folding motion of the AMO cell. Altogether, the kinematics of the AMO cell can be parameterized by $\alpha' \in [0, \alpha]$ or $\gamma \in [0, \pi]$ with $\alpha' = \gamma = 0$ representing the fully folded state, and $\alpha' = \alpha, \gamma = \pi$ representing the flat state.

The AMO cells can be arranged to construct an AMO tessellation, as shown in Fig. 1(d). In the radial direction, the cells are directly replicated. By contrast, in the circumferential direction, the circumferential edge lengths are iteratively enlarged to connect the adjacent unit cells, while the radial edge lengths are kept unchanged. We can see that the AMO tessellation is an axisymmetric structure, and the central angle of an unit cell is equal to double the deviation angle 2δ . When the tessellation is folded, the central angle turns to $2\delta'$, as shown in Fig. 1(e). Therefore, the projected deviation angle δ' is a key variable that reflects the angular motion of the AMO cells and tessellations.

Now we analyze the variation of δ' upon deployment of the AMO cells. As shown in Figs. 1(a)–(c), the projected lengths a' , b' , and d' can be given by

$$a' = a, \quad b' = b \sin \theta, \quad d' = d, \quad (11)$$

where θ is the included angle between a radial edge and the vertical line. Analogous to the Miura cell, the angle θ is related to the deploying parameter α' as follows [51]:

$$\sin \theta = \frac{\cos \alpha}{\cos \alpha'}. \quad (12)$$

Combining Eqs. (4), (8), (11), and (12), we discover an identity in the motion of AMO cells:

$$\frac{\tan \alpha}{\tan \beta} = \frac{\tan \alpha'}{\tan \beta'}. \quad (13)$$

This inspires us to define a geometric invariant of motion by

$$t_{\alpha\beta} = \frac{\tan \alpha}{\tan \beta}, \quad (14)$$

which keeps unchanged for any projected cells on the path of deployment from the fully folded state to the deployed-flat state. We substitute Eqs. (7) and (14) into Eq. (13), and obtain the relationship between the projected deviation angle δ' and the deploying parameter α' :

$$\tan \delta' = \frac{(t_{\alpha\beta} - 1) \tan \alpha'}{t_{\alpha\beta} + \tan^2 \alpha'}. \quad (15)$$

If $t_{\alpha\beta} = 1$, the projected deviation angle δ' is constantly zero. This corresponds to a Miura cell, which always expands simultaneously in two orthogonal in-plane directions upon deployment [51,52]. However, for an AMO cell with $t_{\alpha\beta} > 1$, we will show that the rotational motion in the circumferential direction is not always monotonic. To this end, we use Eq. (15) to calculate the derivative of the projected deviation angle δ' with respect to the deploying parameter α' :

$$\frac{d\delta'}{d\alpha'} = \frac{\cos^2 \delta' (t_{\alpha\beta} - 1)(t_{\alpha\beta} - \tan^2 \alpha')}{\cos^2 \alpha' (t_{\alpha\beta} + \tan^2 \alpha')^2}. \quad (16)$$

Then we can solve $d\delta'/d\alpha' = 0$ to obtain the deploying parameter $\alpha = \alpha^*$, under which the projected deviation angle δ' reaches maximum δ^* :

$$\tan \alpha^* = \sqrt{t_{\alpha\beta}}, \quad (17)$$

$$\tan \delta^* = \frac{1}{2} \left(\sqrt{t_{\alpha\beta}} - \frac{1}{\sqrt{t_{\alpha\beta}}} \right). \quad (18)$$

We can see that the invariant $t_{\alpha\beta}$ determines the extreme value of the projected deviation angle δ^* and the corresponding deploying

parameter α^* . Combining Eqs. (17) and (18), we can further obtain the following relationships:

$$\alpha^* = \frac{\pi}{4} + \frac{\delta^*}{2}, \quad (19)$$

and

$$t_{\alpha\beta} = \tan^2 \left(\frac{\pi}{4} + \frac{\delta^*}{2} \right). \quad (20)$$

In addition, substituting Eq. (10) into Eq. (15), we can determine the relationship between the projected deviation angle δ' and the other deploying parameter γ :

$$\tan \delta' = \frac{(t_{\alpha\beta} - 1) \tan \alpha \sin(\gamma/2)}{t_{\alpha\beta} + \tan^2 \alpha \sin^2(\gamma/2)}. \quad (21)$$

Also, substituting Eqs. (14) and (17) into Eq. (10), we can obtain the deploying parameter γ^* corresponding to the maximum projected deviation angle δ^* :

$$\sin \frac{\gamma^*}{2} = \frac{1}{\sqrt{\tan \alpha \tan \beta}}. \quad (22)$$

We know from Eq. (22) that the existence of a valid extreme point $\gamma^* \in (0, \pi)$ requires $\tan \alpha \tan \beta > 1$, that is, $\pi/2 < \alpha + \beta < \pi$. This condition is equivalent to $\alpha^* < \alpha$, according to Eq. (10). Under this circumstance, the projected deviation angle δ' of an AMO cell will first increase and then decrease upon deployment. Otherwise, it will monotonically decrease to zero from the initial angle δ . According to the values of α and β , we list these two cases below:

- i. $\pi/2 < \alpha + \beta < \pi$
 - The AMO cell has a non-monotonic angular motion.
 - The projected deviation angle $\delta'(\gamma)$ increases on $[0, \gamma^*]$, and decreases on $(\gamma^*, \pi]$, where $\delta'_{\max} = \delta'(\gamma^*) = \delta^*$.
- ii. $0 < \alpha + \beta \leq \pi/2$
 - The AMO cell has a monotonic angular motion.
 - The projected deviation angle $\delta'(\gamma)$ increases on $[0, \pi]$, where $\delta'_{\max} = \delta'(\pi) = \delta$.

Figs. 2(a) and (b) illustrate the variations of the projected deviation angle δ' with respect to the deploying parameter γ for AMO cells with different sector angles. In Fig. 2(a), the major sector angle α is fixed as 0.375π . If the minor sector angle $\beta = 0.125\pi$, the projected deviation angle δ' varies monotonically upon deployment, and reaches a maximum $\delta = 2.5\pi$ at the deployed-flat state with $\gamma = \pi$. By contrast, if β gets larger and satisfies $\alpha + \beta > \pi/2$, the projected deviation angle δ' changes non-monotonically and reaches a maximum at a partially folded state. In Fig. 2(b), the deviation angle δ is fixed as 0.05π . If $\alpha + \beta > \pi/2$, the projected deviation angle δ' varies non-monotonically. Particularly, δ' can reach over three times the deviation angle δ for $\alpha = 0.475$ and $\beta = 0.425$. However, if $\alpha + \beta \leq \pi/2$, the projected deviation angle δ' can only change monotonically in the range $[0, \delta]$.

In the non-monotonic case, we remark that there is no one-to-one match between the projected deviation angle δ' and the folded states of an AMO cell, so that we cannot regard δ' as a deploying parameter. Instead, we use α' or γ because these two angles vary monotonically upon the deployment process. For the same reason, the angle θ can also parameterize the deployment of the unit cell, which will be used in Section 4 to calculate the vertex positions on the folded AMO tessellations.

3. Deployment mechanism of the AMO tessellations

An AMO cell can be deployed from a folded-flat state to a deployed-flat state accompanied with the variation of the projected deviation angle. However, the angular motion of an AMO tessellation is constrained by the condition that the central angle of the tessellation cannot exceed 2π , because the panels are assumed to be undeformable

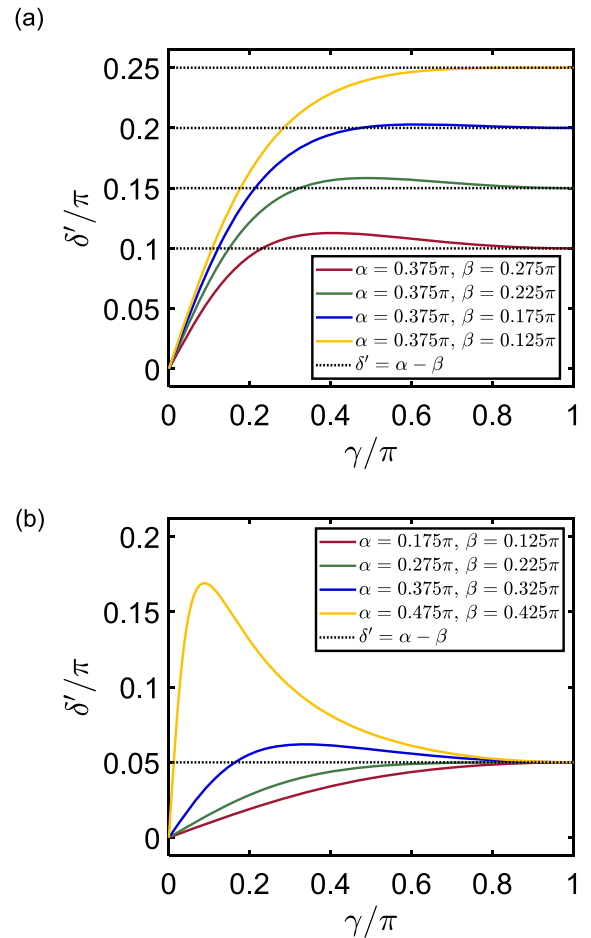


Fig. 2. Variations of the projected deviation angle δ' with respect to the deploying parameter γ for AMO cells with different sector angles. (a) The AMO cells have the same major sector angle α but different minor sector angles β . (b) The AMO cells have the same deviation angle $\delta = \alpha - \beta = 0.05\pi$.

and cannot intersect with each other. If the number of AMO cells replicated in the circumferential direction is large enough, the AMO tessellation may form a closed-ring shape and get locked upon deployment before the cells reach the deployed-flat state. This phenomenon of locking is the vital difference between the deployment behaviors of AMO tessellations and the classical Miura tessellations. In this section, we aim to analyze the locking mechanism of AMO tessellations, and give the corresponding conditions for developability, flat-deployability, and closability. To be clear, we give the following definitions:

- **Developability:** An AMO tessellation has a deployed-flat state without overlap of panels.
- **Flat-deployability:** An AMO tessellation can be rigidly deployed from the folded-flat state to the deployed-flat state, without intersection of panels.
- **Closability:** An AMO tessellation can be rigidly folded from the deployed-flat state, or rigidly deployed from the folded-flat state, to form a closed-ring shape.

We denote the circumferential number of the unit cells by N . Then the developability condition can be written as

$$2N\delta \leq 2\pi, \quad (23)$$

which is equivalent to

$$\alpha - \beta \leq \pi/N. \quad (24)$$

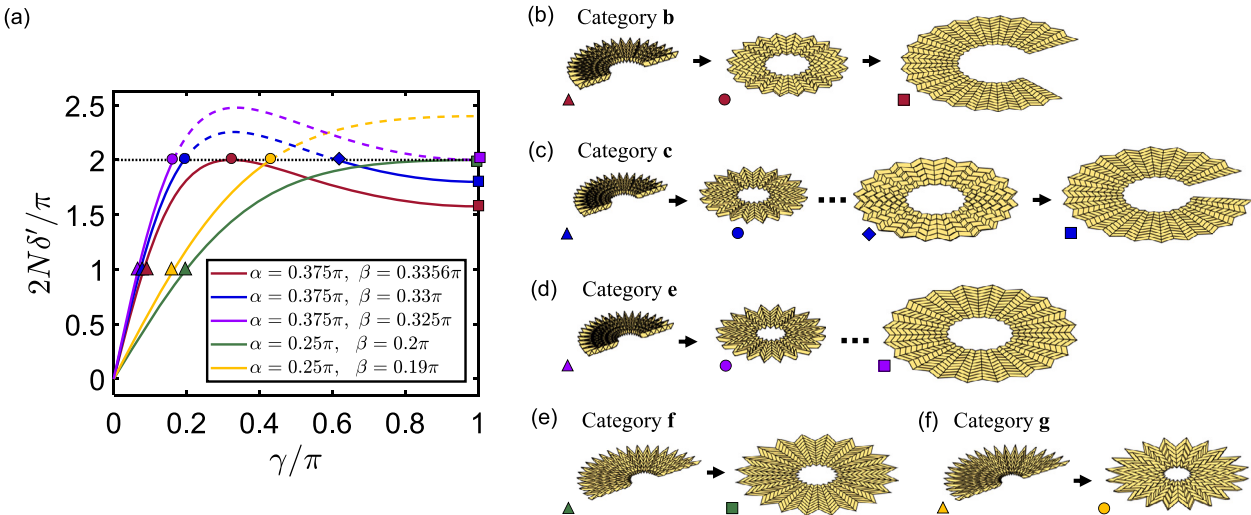


Fig. 3. AMO tessellations that have one or two closed states. (a) Variations of the central angle $2N\delta'$ with respect to the deploying parameter γ , where $N = 20$. The dashed part of a variation curve represents the infeasible region with $2N\delta' > 2\pi$. (b)-(f) Configurations of the AMO tessellations corresponding to the representative points marked on (a).

The flat-deployability condition can be given by

$$2N\delta'_{\max} \leq 2\pi. \quad (25)$$

The closability condition reads

$$2N\delta'_{\max} \geq 2\pi. \quad (26)$$

Obviously, a non-developable AMO tessellation ($\alpha - \beta > \pi/N$) always has a closed state and is non-flat-deployable. By contrast, a developable AMO tessellation composed of unit cells with monotonic angular motion ($\alpha - \beta \leq \pi/N$ and $\alpha + \beta \leq \pi/2$) is always flat-deployable. In particular, if $\alpha - \beta = \pi/N$ and $\alpha + \beta \leq \pi/2$, the developable AMO tessellation has a deployed-flat closed state. Otherwise, if $\alpha - \beta < \pi/N$ and $\alpha + \beta \leq \pi/2$, the deployed-flat state is not closed. In this case, the central angle decreases monotonically upon folding, and therefore the developable AMO tessellation has no closed state.

For a developable AMO tessellation consisting of unit cells with non-monotonic angular motion ($\alpha - \beta \leq \pi/N$ and $\alpha + \beta > \pi/2$), the deployed-flat state cannot always be achieved even though the developability condition is satisfied. For example, if $\alpha - \beta = \pi/N$ and $\alpha + \beta > \pi/2$, the AMO tessellation is developable and has a deployed-flat closed state. But this flat configuration is not rigidly foldable because the central angle cannot exceed 2π . Reversely, the folded-flat AMO tessellation cannot be rigidly deployed to the deployed-flat state as well. In other words, the AMO tessellation is non-flat-deployable. Otherwise, if $\alpha - \beta < \pi/N$ and $\alpha + \beta > \pi/2$, to investigate the corresponding flat-deployability, we need to examine the maximum projected deviation angle of the unit cells from the AMO tessellation. To this end, we substitute $2N\delta^* = 2\pi$ into Eq. (20) and define a geometric invariant of motion:

$$t_N = \tan^2 \left(\frac{\pi}{4} + \frac{\pi}{2N} \right). \quad (27)$$

Firstly, if $t_{\alpha\beta} < t_N$, we have $2N\delta^* < 2\pi$, and therefore the AMO tessellation is flat-deployable and has no closed state. Secondly, if $t_{\alpha\beta} \geq t_N$, we have $2N\delta^* \geq 2\pi$, and the AMO tessellation has one or two closed states. To identify the deploying parameter α' under given δ' , we solve Eq. (15) and obtain

$$\tan \alpha' = \frac{\tan \alpha^*}{\tan \delta'} \left(\tan \delta^* \mp \sqrt{\tan^2 \delta^* - \tan^2 \delta'} \right). \quad (28)$$

For convenience, we introduce the subindexes “1,2” regarding the first and second closed states, respectively. Then we substitute $2N\delta' = 2\pi$ into Eq. (28) and determine the deploying parameters $\alpha' = \bar{\alpha}_{1,2}$ at the closed states:

$$\bar{\alpha}_{1,2} = \arctan \left[\frac{\tan \alpha^*}{\tan(\pi/N)} \left(\tan \delta^* \mp \sqrt{\tan^2 \delta^* - \tan^2 \frac{\pi}{N}} \right) \right], \quad (29)$$

where α^* and δ^* are given by Eqs. (17) and (18), respectively. Furthermore, we combine Eqs. (10), (14), (17), (22), and (29), and then obtain the corresponding deploying parameters $\gamma = \bar{\gamma}_{1,2}$ at the closed states:

$$\bar{\gamma}_{1,2} = 2 \arcsin \left[\frac{\sin(\gamma^*/2)}{\tan(\pi/N)} \left(\tan \delta^* \mp \sqrt{\tan^2 \delta^* - \tan^2 \frac{\pi}{N}} \right) \right], \quad (30)$$

where δ^* and γ^* are given by Eqs. (18) and (22), respectively. For $t_{\alpha\beta} > t_N$, we have $2N\delta^* > 2\pi$ and $\bar{\alpha}_1 < \bar{\alpha}_2$, indicating that the AMO tessellation is non-flat-deployable and has two closed states. For $t_{\alpha\beta} = t_N$, we have $2N\delta^* = 2\pi$ and $\bar{\alpha}_1 = \bar{\alpha}_2$, which corresponds to a single closed state. In this case, the AMO tessellation can be deployed to form a closed-ring shape with an increase of the central angle from 0 to 2π , and then to the deployed-flat state with a decrease of the central angle from 2π to $2N\delta$. The tessellation does not get locked at the closed state because the central angle will decrease immediately after it reaches 2π . Thus, the AMO tessellation satisfying $t_{\alpha\beta} = t_N$ is developable, flat-deployable, and closable.

Altogether, we can classify the AMO tessellations into seven categories as below:

- a. $\alpha - \beta < \pi/N, \alpha + \beta > \pi/2, t_{\alpha\beta} < t_N, 0 < \beta < \alpha < \pi/2$.
 - The AMO tessellation is developable, flat-deployable, and unclosable.
- b. $\alpha - \beta < \pi/N, \alpha + \beta > \pi/2, t_{\alpha\beta} = t_N, 0 < \beta < \alpha < \pi/2$.
 - The AMO tessellation is developable, flat-deployable, and closable at one folded state.
 - The central angle $2N\delta'(\gamma)$ increases on $[0, \gamma^*]$, and decreases on $(\gamma^*, \pi]$, where the maximum central angle is $2N\delta'(\gamma^*) = 2N\delta^* < 2\pi$.
- c. $\alpha - \beta < \pi/N, \alpha + \beta > \pi/2, t_{\alpha\beta} > t_N, 0 < \beta < \alpha < \pi/2$.
 - The AMO tessellation is developable, non-flat-deployable, and closable at two folded states.
 - The central angle $2N\delta'(\gamma)$ increases on $[0, \bar{\gamma}_1]$, and decreases on $[\bar{\gamma}_2, \pi]$, where the maximum central angle is $2N\delta'(\bar{\gamma}_{1,2}) = 2N\delta^* = 2\pi$.
- d. $\alpha - \beta < \pi/N, \alpha + \beta \leq \pi/2, 0 < \beta < \alpha < \pi/2$.
 - The AMO tessellation is developable, flat-deployable, and unclosable.
 - The central angle $2N\delta'(\gamma)$ increases on $[0, \pi]$, where the maximum central angle is $2N\delta'(\pi) = 2N\delta < 2\pi$.
- e. $\alpha - \beta = \pi/N, \alpha + \beta > \pi/2, 0 < \beta < \alpha < \pi/2$.
 - The AMO tessellation is developable, non-flat-deployable, and closable at one folded state and the deployed-flat state.
 - The central angle $2N\delta'(\gamma)$ increases on $[0, \bar{\gamma}_1]$, and is an isolated point at $\bar{\gamma}_2 = \pi$, where the maximum central angle is $2N\delta(\bar{\gamma}_{1,2}) = 2\pi$.

- f. $\alpha - \beta = \pi/N$, $\alpha + \beta \leq \pi/2$, $0 < \beta < \alpha < \pi/2$.
 - The AMO tessellation is developable, flat-deployable, and closable at the deployed-flat state.
 - The central angle $2N\delta'(\gamma)$ increases on $[0, \pi]$, where the maximum central angle is $2N\delta'(\pi) = 2N\delta = 2\pi$.
- g. $\alpha - \beta > \pi/N$, $0 < \beta < \alpha < \pi/2$.
 - The AMO tessellation is non-developable, non-flat-deployable, and closable at one folded state.
 - The central angle $2N\delta'(\gamma)$ increases on $[0, \bar{\gamma}_1]$, where the maximum central angle is $2N\delta'(\bar{\gamma}_1) = 2\pi$.

Among the seven categories above, the AMO tessellations have two closed states in categories **c** and **e**, one closed state in categories **b**, **f**, and **g**, and no closed state in categories **a** and **d**. Remind that we have solved Eq. (15) under the condition $2N\delta' = 2\pi$ to obtain Eq. (30), which gives the expressions of deploying parameters $\gamma = \bar{\gamma}_{1,2}$ at the closed states of AMO tessellations in categories **b** and **c**. The derivation can be directly generalized to all the closable AMO tessellations in categories **b**, **c**, **e**, **f**, and **g**. Following the same procedure, we can obtain the expression of deploying parameter $\gamma = \bar{\gamma}_1$ at the first closed state of these tessellations:

$$\bar{\gamma}_1 = 2 \arcsin \left[\frac{\sin(\gamma^*/2)}{\tan(\pi/N)} \left(\tan \delta^* - \sqrt{\tan^2 \delta^* - \tan^2 \frac{\pi}{N}} \right) \right], \quad (31)$$

where δ^* and γ^* are given by Eqs. (18) and (22), respectively. In other words, for any closable AMO tessellation, there always exists the first closed state with $\gamma = \bar{\gamma}_1$. The difference lies in the second closed state corresponding to $\gamma = \bar{\gamma}_2$: in category **b**, we have $\bar{\gamma}_2 = \bar{\gamma}_1$; in categories **c** and **e**, we have $\bar{\gamma}_2 > \bar{\gamma}_1$; in categories **f** and **g**, $\bar{\gamma}_2$ does not exist. In Fig. 3(a), we illustrate the variations of the central angle $2N\delta'$ with respect to the deploying parameter γ for typical examples from the five categories of AMO tessellations that have one or two closed states. These AMO tessellations have the same number of circumferential cells $N = 20$, but different major sector angles α and minor sector angles β . The configurations of these AMO tessellations are shown in Figs. 3(b)–(f), corresponding to categories **b**, **c**, **e**, **f**, and **g**, respectively.

Despite adjusting the major and minor sector angles, we can also change the number of unit cells to obtain AMO tessellations with various deployment behaviors. Fig. 4(a) illustrates the variations of the central angle $2N\delta'$ with respect to the deploying parameter γ for AMO tessellations composed of different numbers of circumferentially replicated unit cells. The unit cells have the same sector angles $\alpha = 0.375\pi$ and $\beta = 0.325\pi$, corresponding to a non-monotonic angular motion (category **i**). When $N = 14$, the central angle $2N\delta'$ is always less than 2π , and the AMO tessellation has no closed state (category **a**). As N increases to 17, the central angle $2N\delta'$ can reach 2π , and the AMO tessellation has two folded closed states (category **c**). If $N = 20$, we have $2N\delta = 2N(\alpha - \beta) = 2\pi$, and therefore the second closed state becomes isolated and flat (category **e**). The circumferential cell number N is further increased to 23 such that $2N\delta = 2N(\alpha - \beta) > 2\pi$. In this case, the AMO tessellation is non-flat-deployable and has one folded closed state (category **g**). Additionally, in Fig. 4(b), we show the variations of the central angle when the unit cells have a monotonic angular motion with $\alpha = 0.25\pi$ and $\beta = 0.2\pi$. When $N = 14$ and 17, the AMO tessellations have no closed state (category **d**). As N increases to 20, we have $2N\delta = 2N(\alpha - \beta) = 2\pi$, corresponding to a flat-deployable AMO tessellation with a deployed-flat closed state (category **f**). Finally, if $N = 23$, the AMO tessellation has one folded closed state (category **g**).

4. Doubly curved AMO tessellations

So far, we have formulated the angular motion of AMO tessellations. The radial edge lengths are kept unchanged when the unit cells are tessellated along the radial direction. Therefore, the upper (or lower) vertices of the tessellations remain in a planar surface

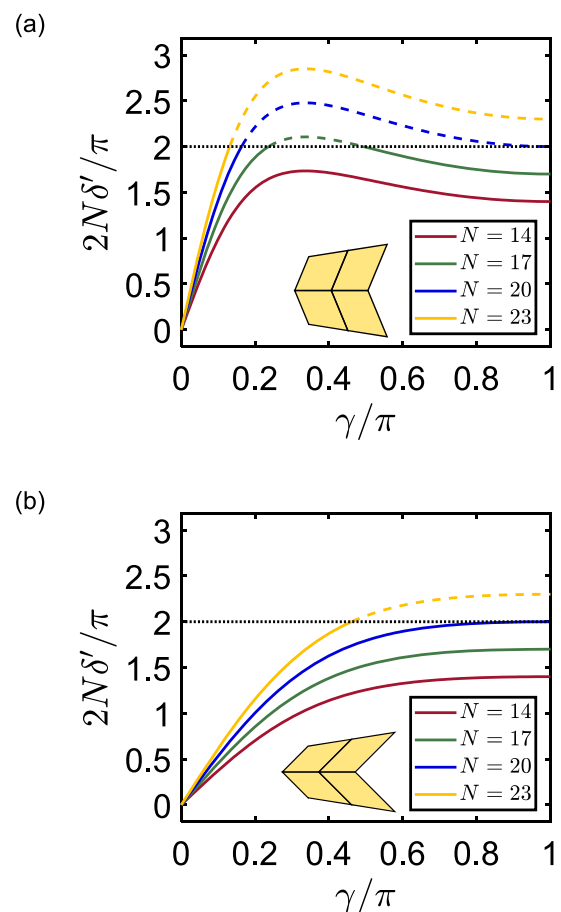


Fig. 4. Variations of the central angle $2N\delta'$ with respect to the deploying parameter γ for AMO tessellations composed of different numbers of circumferentially replicated unit cells. The dashed part of a variation curve represents the infeasible region with $2N\delta' > 2\pi$. (a) The unit cell has a non-monotonic angular motion with $\alpha = 0.375\pi$ and $\beta = 0.325\pi$. (b) The unit cell has a monotonic angular motion with $\alpha = 0.25\pi$ and $\beta = 0.2\pi$.

upon folding, while curved shapes are formed in the circumferential direction. We call this type of AMO tessellations the *singly curved AMO tessellations*. If we modify the radial edge lengths, the upper (or lower) vertices of a folded AMO tessellation will not stay planar, but otherwise, constitute a discrete curved surface. The modified AMO tessellations can be named the *doubly curved AMO tessellations*. In addition, the radial edge lengths can be optimized to design AMO tessellations that approximate a target surface of revolution at the folded closed state. Explorations on this shape-morphing problem can be found in [46,47]. The examples provided in [46] are developable and flat-deployable (category **b**). By contrast, the examples in [47] are developable and non-flat-deployable (category **c**). However, the sector angles α and β are outputs of the inverse design algorithms in [46,47]; therefore the deployment kinematics of the AMO tessellations cannot be precisely designed on demand. To overcome this issue, we develop an easy-to-implement optimization framework for the shape morphing of closed AMO tessellations. The deployment kinematics can be fixed in advance, and the radial edge lengths are optimized to minimize the distance between a target surface and the upper (or lower) vertices of an AMO tessellation.

4.1. Kinematics

To begin with, we formulate the vertex positions of doubly curved AMO tessellations upon deployment. An AMO strip with five unit cells

Table 1
Geometric parameters for doubly curved AMO tessellations.

Row	M	N	α	β	δ	$\bar{\alpha}_1$	a	h	b_1, b_2, \dots, b_{10}	γ
1	5	40	0.375π	0.35π	0.025π	0.15π	0.6	1.42	0.9, 1.1, 0.8, 1.2, 0.7, 1.3, 0.6, 1.4, 0.5, 1.5 0.939, 1.252, 0.856, 1.310, 0.773, 1.362, 0.691, 1.406, 0.611, 0.144	0.1354 π
2	5	40	0.375π	0.3563π	0.01868π	0.2625π	0.231	0.16	1.277, 1.559, 1.205, 1.615, 1.132, 1.667, 1.058, 1.715, 0.985, 1.758	0.2958 π
3	5	40	0.375π	0.35π	0.025π	0.15π	0.41	0.16	1.277, 1.559, 1.205, 1.615, 1.132, 1.667, 1.058, 1.715, 0.985, 1.758	0.1354 π

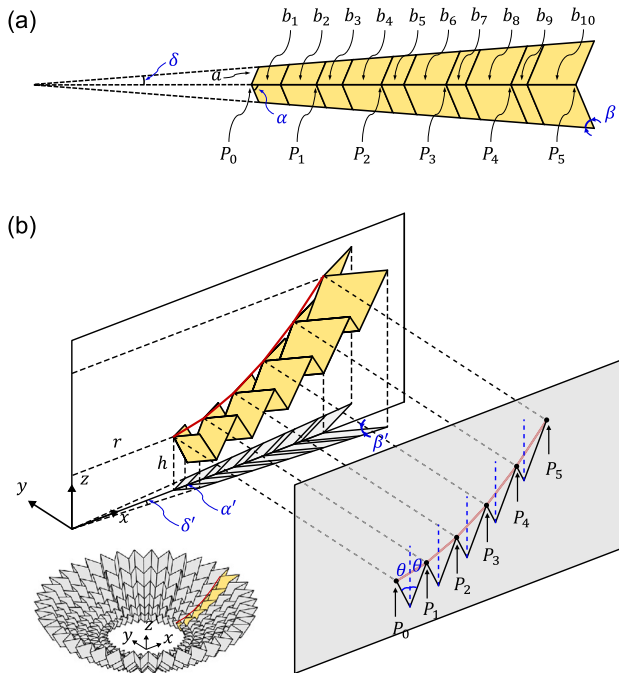


Fig. 5. Doubly curved AMO tessellation. (a) An AMO strip composed of five unit cells with different radial edge lengths. (b) The folded AMO strip can be placed in a coordinate system where the zx -plane serves as a plane of symmetry. In addition, the strip can be circumferentially replicated to construct a doubly curved AMO tessellation with the upper vertices forming a discrete surface of revolution (bottom left).

of different radial edge lengths is illustrated in Fig. 5(a). The strip can be characterized by the major sector angle α , the minor sector angle β , the circumferential edge length a , and the array of radial edge lengths $(b_1, b_2, \dots, b_{10})$. The deviation angle δ is half the central angle of the tapered strip. We also illustrate a folded state of this AMO tessellation and the corresponding projected pattern in Fig. 5(b). The included angle between a radial edge and the z -axis is denoted by θ . The projected pattern on the xy -plane is also a tapered strip. The projected major and minor sector angles are denoted by α' and β' , respectively. The projected deviation angle δ' is half the central angle of the projected tapered strip. The upper vertices P_0, P_1, \dots, P_5 of the folded strip can be linked to form a curved line in the xz -plane. Since the angular motion of the unit cells only depends on the sector angles α and β , the kinematic formulations of the projected angles α' and δ' are the same as the singly curved case, despite that the radial edge lengths are not identical with each other. As a result, the criteria for developability, flat-deployability, closability, as well as the categories **a–g** for singly curved tessellations, can be applied to doubly curved tessellations straightforwardly.

In general, for an AMO strip with M unit cells in the radial direction, we denote the radial edge lengths by $\tilde{\mathbf{b}} = (b_1, b_2, \dots, b_{2M})$, and the upper-side vertices by P_0, P_1, \dots, P_M . As shown in Fig. 5(b), a Cartesian coordinate system $O - xyz$ is built such that the x -axis is the axis of symmetry of the projected strip, and the z -axis is the axis of rotational symmetry of the folded AMO tessellation. As a result, the vertices P_k are

in the xz plane. We further denote the height of the innermost vertex P_0 by h . Thus, the coordinates of P_0 are given by

$$x_0 = a \frac{\sin \beta'}{\sin \delta'}, \quad y_0 = 0, \quad z_0 = h. \quad (32)$$

Then, the positions of other vertices P_k on the upper side can be calculated iteratively by

$$\begin{cases} x_k = x_{k-1} + (b_{2k} + b_{2k-1}) \sin \theta, \\ y_k = 0, \\ z_k = z_{k-1} + (b_{2k} - b_{2k-1}) \cos \theta, \end{cases} \quad (33)$$

for $k = 1, 2, \dots, M$, where the angle θ is dependent on the deploying parameter α' and major sector angle α as given in Eq. (12). To be clear, the angle θ is always the same for every unit cell in the tessellation, because the angles α' and α are identical from cell to cell. From Eqs. (32) and (33), we can see that the vertex positions (x_k, y_k, z_k) can be modified by altering the length parameters a , h , and $\tilde{\mathbf{b}}$ under fixed projected angles α' , β' , and δ' , for $k = 0, 1, \dots, M$. Therefore, we can design the closed shape of an AMO tessellation with fixed angular deployment kinematics.

4.2. Approximating surfaces of revolution

In light of the rotational symmetry, the shape design of an $M \times N$ AMO tessellation can be simplified to the design of a strip extracted from the tessellation, i.e., to minimize the distance between the generatrix of the target surface and the upper (or lower) vertices on the strip. We denote the target generatrix by $z = f(x)$, $x \in [r, R]$ and the upper vertices by P_k . To initialize the inverse design of AMO tessellations, we choose the geometric parameters M , N , α , and β from one of the categories **b**, **c**, **e**, **f**, and **g**. Considering that the deploying parameters α' and γ have a one-to-one correspondence given by Eq. (10), we can use Eq. (31) to derive the expression of the deploying parameter $\alpha' = \bar{\alpha}_1$ at the first closed state:

$$\bar{\alpha}_1 = \arctan \left[\frac{\tan \alpha^*}{\tan(\pi/N)} \left(\tan \delta^* - \sqrt{\tan^2 \delta^* - \tan^2 \frac{\pi}{N}} \right) \right]. \quad (34)$$

The aim is to determine the vertices P_k , such that they locate on the generatrix $z = f(x)$ and cover the range from $x_0 = r$ to $x_M = R$. To this end, firstly, we fix the location of the innermost vertex P_0 as the left endpoint $(r, 0, f(r))$ of the generatrix. Since the projected angles are $\delta' = \pi/N$ and $\beta' = \bar{\alpha}_1 - \pi/N$ for the closed configuration, the parameters a and h can be solved from Eq. (32):

$$a = r \frac{\sin(\pi/N)}{\sin(\bar{\alpha}_1 - \pi/N)}, \quad h = f(r). \quad (35)$$

The other vertices P_k on the upper side of the strip can be calculated by Eq. (33) in terms of the radial edge lengths $\tilde{\mathbf{b}} = (b_1, b_2, \dots, b_{2M})$ and the deploying parameter

$$\theta = \arcsin \left(\frac{\cos \alpha}{\cos \bar{\alpha}_1} \right). \quad (36)$$

Secondly, we determine the radial edge lengths $\tilde{\mathbf{b}}$ by solving the following optimization problem:

$$\min_{\tilde{\mathbf{b}}} \text{Var}(\tilde{\mathbf{b}}) \text{ subject to } \begin{cases} |f(x_k) - z_k| = 0 \\ |x_M - R| = 0 \end{cases}, \quad (37)$$

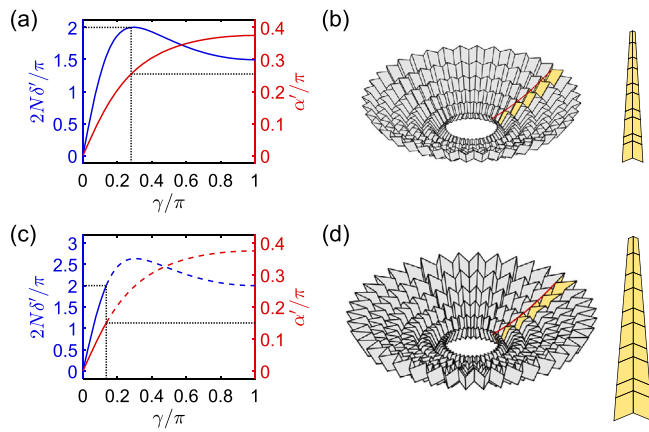


Fig. 6. Doubly curved AMO tessellations ($N = 40$) that are optimized to approximate a parabolic surface. (a) and (c) The variations of the central angle $2N\delta'$ and the deploying parameter α' with respect to the deploying parameter γ for the prescribed angular motion. (b) and (d) The closed ring-like configurations and the origami patterns of the deployed-flat strips that are optimized based on the angular motion in (a) and (c), respectively. The AMO tessellation in (b) is flat-deployable, and the AMO tessellation in (d) is non-flat-deployable. The dashed part of a variation curve represents the infeasible region with $2N\delta' > 2\pi$ or $\alpha' > \bar{\alpha}_1$.

where $\text{Var}(\tilde{\mathbf{b}})$ is the variance of $\tilde{\mathbf{b}}$, defined as

$$\text{Var}(\tilde{\mathbf{b}}) = \frac{1}{2M} \sum_{i=1}^{2M} (b_i - \mu)^2, \quad \mu = \frac{1}{2M} \sum_{i=1}^{2M} b_i. \quad (38)$$

In this optimization, we utilize the objective function $\text{Var}(\tilde{\mathbf{b}})$ to achieve a relatively uniform distribution of radial edge lengths.

Fig. 6 illustrates two examples of 5×40 AMO tessellations that approximate a parabolic surface with the generatrix $y = 0.04x^2$, $x \in [2, 8]$. In the first example, the sector angles α, β are assigned to generate a flat-deployable AMO tessellation (category b), as shown in Figs. 6(a) and (b). In the second example, the AMO tessellation is specified to be non-flat-deployable (category e), as shown in Fig. 6(c) and (d). We solve Eq. (37) to obtain the corresponding radial edge lengths. It can be observed that the designed AMO strips are different in sizes and shapes, but the assembled tessellations can form the same target shape at the folded closed configurations. The geometric and deploying parameters of these two AMO tessellations are listed in the second and third rows of Table 1. Note that in this section we have used $\alpha' = \bar{\alpha}_1$ to represent the closed states of AMO tessellations. This is equivalent to $\gamma = \bar{\gamma}_1$, because α' and γ have a one-to-one correspondence with each other. Each of the conditions $\alpha' = \bar{\alpha}_1$ and $\gamma = \bar{\gamma}_1$ indicates that the AMO tessellations form a closed configuration with $2N\delta' = 2\pi$. As a result, the infeasible region of deployment (e.g., the dashed part in 6(c)) can be described by either $2N\delta'(\gamma) > 2\pi$ or $\alpha'(\gamma) > \bar{\alpha}_1$.

5. Multi-layer stacked metamaterials

Classical Miura origami tessellations can be stacked to build deployable 3D metamaterials [51,64,65]. As a generalization, a deployable two-layer configuration of doubly curved AMO tessellations was presented in [46]. However, the conditions for the deployability of stacked AMO tessellations have not been fully explored. In this section, we aim to systematically show how to design deployable stacked metamaterials with singly and doubly curved AMO tessellations. We will also reveal the discrepancy of stacked deployability between singly and doubly curved AMO tessellations.

5.1. Singly curved case

We start by investigating the combination of two singly curved AMO cells. Analogous to other stacked origami metamaterials with degree-4 vertices [64,65], the two layers of AMO cells can be stacked into

nested-in or bulged-out configurations. We demonstrate the AMO cells corresponding to these two stacking modes in Fig. 7(a). If the stacked unit cells can be deployed simultaneously, the motion of connected edges should keep coincident on the path of deployment. Therefore, the unit cells share the same projected patterns, as illustrated in Figs. 7(c) and (d). Furthermore, we can see that a nested-in counterpart of a given AMO cell A can be transferred to a bulged-out one by simply reversing the orientation of placement. As a result, basically, we can formulate the deployment kinematics of the nested-in and bulged-out configurations of singly curved AMO cells using the same equations. We use the notations in Figs. 1(a)–(c) to denote the geometric and deploying parameters of the two layers of AMO cells, and distinguish them by the superscripts A and B, as shown in Figs. 7(c) and (d). Since the stacked cells in layers A and B have the same projected pattern, they have the same projected angles α', β', δ' and edge lengths a', b' . Then we can examine the deployment kinematics of the stacked cells from Eqs. (11)–(13), and obtain the following constraints for stacking:

$$\frac{\tan \alpha'}{\tan \beta'} = \frac{\tan \alpha^A}{\tan \beta^A} = \frac{\tan \alpha^B}{\tan \beta^B}, \quad (39)$$

$$a' = a^A = a^B, \quad (40)$$

$$b' \cos \alpha' = b^A \cos \alpha^A = b^B \cos \alpha^B. \quad (41)$$

Eqs. (39)–(41) give the geometric conditions for the deployability of stacked singly curved AMO cells in layers A and B. In addition, we can use Eq. (10) to obtain the relationship between the deploying parameters for these two cells:

$$\tan \alpha' = \sin \frac{\gamma^A}{2} \tan \alpha^A = \sin \frac{\gamma^B}{2} \tan \alpha^B. \quad (42)$$

We note that Eqs. (39)–(42) can also apply to stacked Miura cells [51]. In particular, Eq. (39) becomes an identity $\alpha' \equiv \beta'$ because we have $\alpha^A = \beta^A$ and $\alpha^B = \beta^B$ for Miura cells.

In analogy with the single-layer AMO tessellations, the stacked tessellations can be built by arranging the stacked cells in layers A and B in the radial and circumferential directions. Then we can alternate the tessellations in layers A and B along the altitude direction to construct the multi-layer stacked metamaterials, as shown in Figs. 8(a) and (b). Note that we can also construct metamaterials stacked by singly curved AMO tessellations varying from layer to layer, as long as the adjacent layers of the AMO tessellations satisfy the constraints given by Eqs. (39)–(41). For brevity, we only discuss the basic configurations of alternate layers.

The deployment kinematics of a separate tessellation extracted from the stacked metamaterials follow the classifications in categories a–g. However, the synchronous motion of the stacked metamaterials is constrained by the condition that the AMO tessellations of each layer share the same projected pattern on the deployment path. In other words, the deployment of the stacked metamaterials can only happen at the overlapping range of the deploying parameters α' for the AMO tessellations in each layer. For example, consider the nested-in stacked metamaterial in Fig. 8(a). The AMO tessellations in layers A and B have the geometric parameters $\alpha^A = 0.3623\pi$, $\beta^A = 0.3423\pi$, $\alpha^B = 0.275\pi$, $\beta^B = 0.25\pi$, and $N = 40$. Therefore, the deployment kinematics of the tessellations in layers A and B drop in categories b and f, respectively, that is, both the tessellations are developable and flat-deployable, but the tessellation A has a folded closed state while the tessellation B has a deployed-flat closed state. The variations of the deploying parameter γ with respect to the deploying parameter α' for the AMO cells in layers A and B are plotted in Fig. 8(c). Recall that, for the flat-deployable AMO tessellation in layer A (or B), γ varies from 0 to π with α' increasing from 0 to α^A (or α^B) on the entire path of deployment from the folded-flat state to the deployed-flat state. One can observe from Fig. 8(c) that when the tessellation B is deployed-flat at $\alpha' = \alpha^B$, the tessellation A is still partially folded. However,

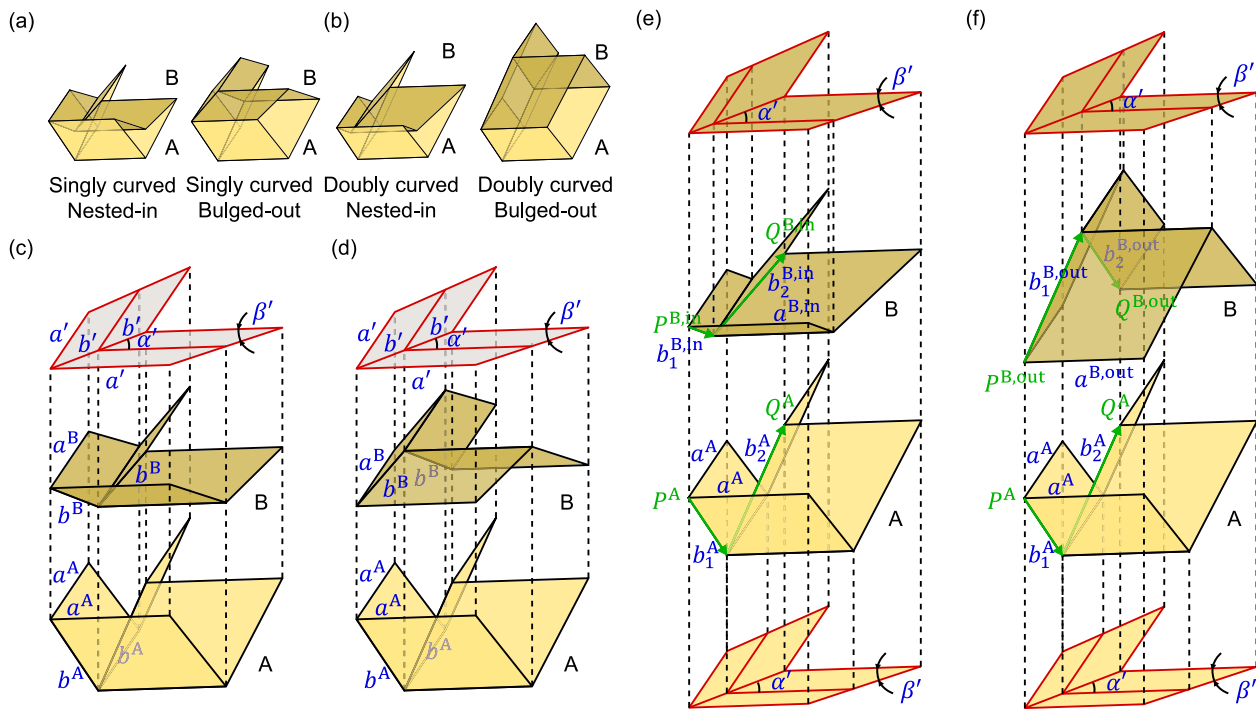


Fig. 7. Stacked AMO cells. (a) The nested-in and bulged-out stacked configurations of singly curved cells. (b) The nested-in and bulged-out stacked configurations of doubly curved cells. (c) and (d) The singly curved cells in a stacked configuration have the same projected pattern. (e) and (f) The doubly curved cells in a stacked configuration have projected patterns with the same outlines but different radial edge lengths.

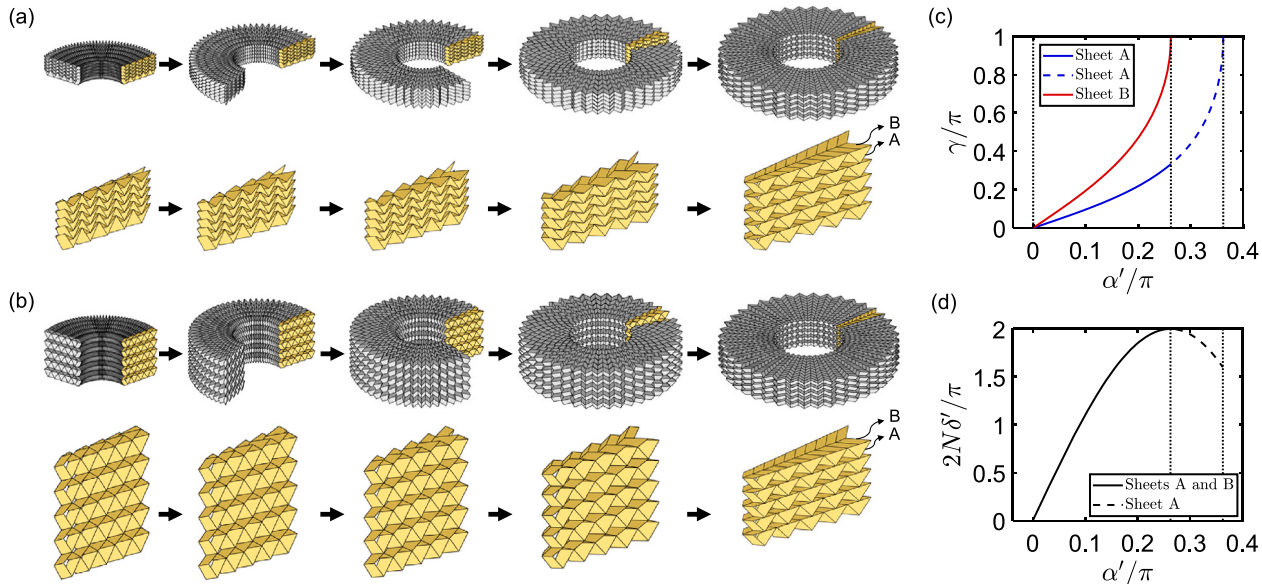


Fig. 8. Singly curved stacked AMO metamataterials that have a locking mechanism at the closed ring-like state. (a) Deployment of the nested-in configuration. (b) Deployment of the bulged-out configuration. (c) The variations of the deploying parameter γ with respect to the deploying parameter α' for the tessellations in layers A and B. (d) The variations of the central angle $2N\delta'$ with respect to the deploying parameter α' for the tessellations in layers A and B. The dashed lines in (c) and (d) represent the infeasible region for the tessellations in layers A.

the stacked metamaterial cannot be further deployed from $\alpha' = \alpha^B$ to $\alpha' = \alpha^A$ because the deploying parameter α' cannot exceed the range of tessellation B. As a result, the stacked metamaterials are non-flat-deployable. In addition, the variations of the central angle $2N\delta'$ with respect to the deploying parameter α' are plotted in Fig. 8(d). The central angle starts to increase at 0 and finally stops at 2π , which indicates that the stacked metamaterial gets locked at the folded closed state despite that a single tessellation in layer A can be further deployed

with a decrease of the central angle. This phenomenon can also be seen in the bulged-out stacked metamaterial as shown in Fig. 8(b).

Generally, we can construct axisymmetric origami metamaterials with a locking mechanism by stacking two successive layers of developable AMO tessellations that do not exhibit locking behaviors. The developability provides convenience for the manufacture of these tessellations. In such metamaterials, the folded closed state of a tessellation in layer A (category b) should match the deployed-flat closed state

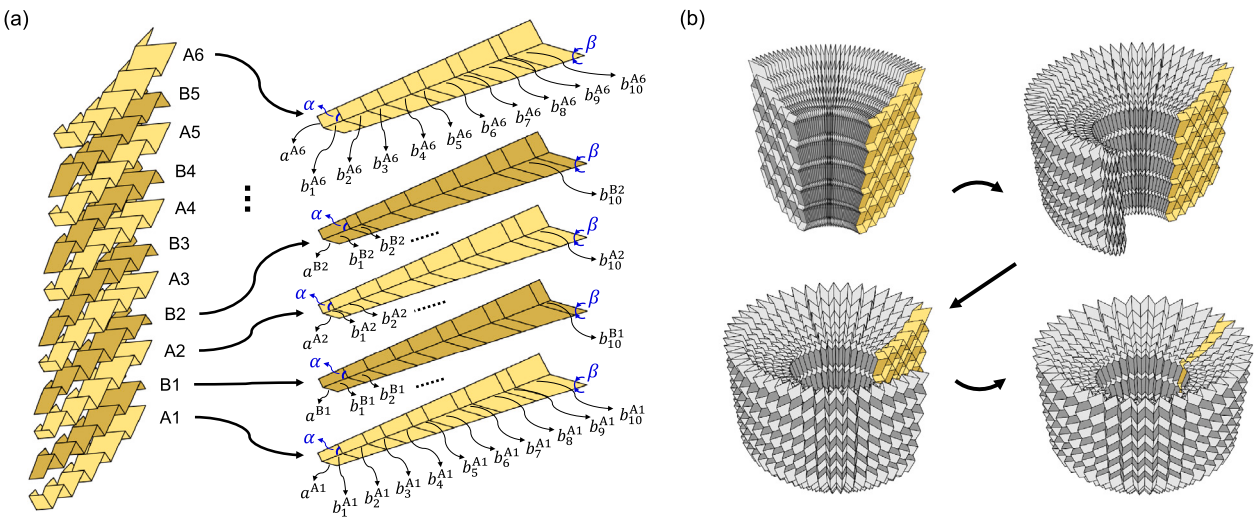


Fig. 9. A deployable metamaterial with a locking mechanism at the closed ring-like state. The metamatetrial is in a bulged-out stacked configuration and composed of eleven layers of 10×40 doubly curved AMO tessellations. (a) Geometric notations of the tapered strips extracted from the tessellations in each layer of the metamatetrial. The major and minor sector angles are $\alpha = 0.375\pi$ and $\beta = 0.35\pi$, respectively. (b) Deployment process of the stacked metamatetrial.

of the tessellation in layer B (category f), which can be formulated as

$$\alpha^{*,A} = \alpha^B = \frac{\pi}{4} + \frac{\pi}{2N}, \quad (43)$$

where $\alpha^{*,A}$ is the extreme point of the deploying parameter α' for the AMO tessellation in layer A, as defined in Eq. (17). Combining Eqs. (17), (39), and (43), we obtain

$$\tan \frac{\alpha^A}{\tan \beta^A} = \tan^2 \left(\frac{\pi}{4} + \frac{\pi}{2N} \right), \quad (44)$$

and

$$\alpha^B = \frac{\pi}{4} + \frac{\pi}{2N}, \quad \beta^B = \frac{\pi}{4} - \frac{\pi}{2N}. \quad (45)$$

Eqs. (44) and (45), together with Eqs. (39)–(41), give the constraints for stacking the developable and flat-deployable AMO tessellations to build axisymmetric origami metamaterials with a locking mechanism.

5.2. Doubly curved case

Now we switch to the stacked cells of doubly curved AMO tessellations, which also include nested-in and bulged-out configurations, as shown in Fig. 7(b). In analogy with the singly curved case, the circumferential edges on the boundaries in adjacent layers should connect with each other correspondingly to compose a stacked configuration. Therefore, the stacked constraints should include Eqs. (39) and (40). However, a doubly curved AMO cell has different radial edge lengths, which means that we cannot obtain a bulged-out stacked configuration by simply reversing the placement of a nested-in cell. As a result, the stacked constraints for the radial edge lengths of doubly curved AMO cells should be formulated separately for nested-in and bulged-out configurations.

We use the notations in Fig. 7(e) to denote the geometric parameters of the nested-in stacked cells and their projected patterns. For a stacked configuration, the vertices P^A and Q^A should coincide with $P^{B,\text{in}}$ and $Q^{B,\text{in}}$ respectively, which can be written as

$$\overline{P^A Q^A} = \overline{P^{B,\text{in}} Q^{B,\text{in}}}. \quad (46)$$

Furthermore, using the kinematic formulations given by Eqs. (12) and (33), we can obtain the component expressions of Eq. (46) in the horizontal and vertical directions:

$$(b_1^A + b_2^A) \frac{\cos \alpha^A}{\cos \alpha'} = (b_1^{B,\text{in}} + b_2^{B,\text{in}}) \frac{\cos \alpha^{B,\text{in}}}{\cos \alpha'}, \quad (47)$$

$$(b_1^A - b_2^A) \sqrt{1 - \frac{\cos^2 \alpha^A}{\cos^2 \alpha'}} = (b_1^{B,\text{in}} - b_2^{B,\text{in}}) \sqrt{1 - \frac{\cos^2 \alpha^{B,\text{in}}}{\cos^2 \alpha'}}. \quad (48)$$

Since we have $b_1^A \neq b_2^A$ and $b_1^{B,\text{in}} \neq b_2^{B,\text{in}}$ for doubly curved cells, Eq. (48) holds for varying α' if and only if $\alpha^A = \alpha^{B,\text{in}}$. In this case, we obtain

$$b_1^A = b_1^{B,\text{in}} \quad \text{and} \quad b_2^A = b_2^{B,\text{in}} \quad (49)$$

by solving Eqs. (47) and (48), which means that a nested-in stacked configuration of doubly curved AMO cells is deployable if and only if the two cells are identical with each other. However, the nested-in stacking of two identical cells is invalid because a complete overlap of two cells will occur on the entire deployment path of such stacking configurations. As a result, we conclude that any nested-in stacked configuration of doubly curved AMO cells is non-deployable.

For the bulged-out stacked configurations, we use the notations in Fig. 7(f) to describe the geometry. The stacking constraint given by Eq. (40) can be rewritten as

$$a^A = a^{B,\text{out}}, \quad (50)$$

and the stacking constraint for radial edges is given by

$$\overline{P^A Q^A} = \overline{P^{B,\text{out}} Q^{B,\text{out}}}. \quad (51)$$

Similar to Eqs. (47) and (48), we write the component expressions of Eq. (51):

$$(b_1^A + b_2^A) \frac{\cos \alpha^A}{\cos \alpha'} = (b_1^{B,\text{out}} + b_2^{B,\text{out}}) \frac{\cos \alpha^{B,\text{out}}}{\cos \alpha'}, \quad (52)$$

$$(b_1^A - b_2^A) \sqrt{1 - \frac{\cos^2 \alpha^A}{\cos^2 \alpha'}} = (b_1^{B,\text{out}} - b_2^{B,\text{out}}) \sqrt{1 - \frac{\cos^2 \alpha^{B,\text{out}}}{\cos^2 \alpha'}}. \quad (53)$$

Again, we have $b_1^A \neq b_2^A$ and $b_1^{B,\text{out}} \neq b_2^{B,\text{out}}$ for doubly curved cells, and $\alpha^A = \alpha^{B,\text{out}}$ for a deployable stacked configuration. Then we solve Eqs. (52) and (53) to determine the relationships for the radial edge lengths:

$$b_1^A = b_2^{B,\text{out}} \quad \text{and} \quad b_2^A = b_1^{B,\text{out}}. \quad (54)$$

Eq. (54) indicates that a bulged-out stacked configuration of doubly curved AMO cells are deployable if and only if the radial edge lengths in layer A are equal to those in layer B but have a reverse order. In addition, substituting $\alpha^A = \alpha^{B,\text{out}}$ into Eq. (39), we obtain

$$\alpha^A = \alpha^{B,\text{out}} \quad \text{and} \quad \beta^A = \beta^{B,\text{out}}. \quad (55)$$

Altogether, Eqs. (50), (54), and (55) give the geometric constraints for the deployability of bulged-out stacked configurations of doubly curved AMO cells.

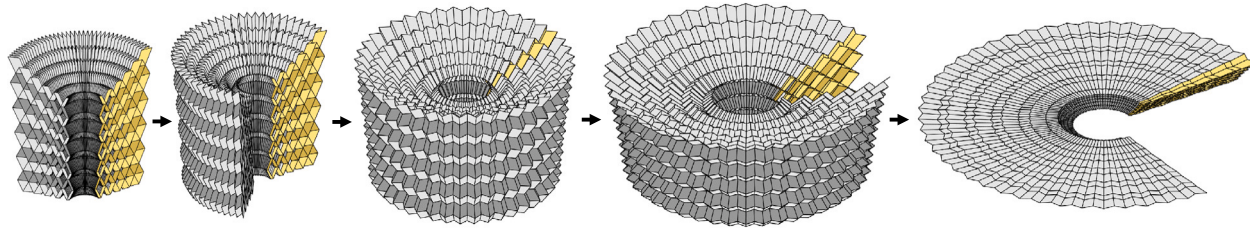


Fig. 10. The deployment process of a flat-deployable metamaterial. The metamaterial is in a bulged-out stacked configuration and composed of eleven layers of 10×40 doubly curved AMO tessellations. The major and minor sector angles are $\alpha = 0.375\pi$ and $\beta = 0.3563\pi$, respectively.

From the discussions above, we know that the deployable multi-layer metamaterials composed of doubly curved AMO tessellations can only have bulged-out configurations. We use the notations in Fig. 9(a) to describe the geometry of the bulged-out stacked tessellations. The layers of tessellations are indexed from bottom to top by A1, B1, A2, B2, A3, etc. According to Eq. (55), the sector angles of the tessellations in each layer should be the same, denoted by α and β . In general, we denote the unit cell numbers in the radial and circumferential directions by M and N , respectively. Then we can apply Eq. (54) to the radial edges in adjacent layers, and obtain the following relationships:

$$b_j^{Bi} = b_{j+1}^{Ai}, \quad j = 1, 3, \dots, 2M - 1, \quad (56)$$

$$b_j^{Bi} = b_{j-1}^{Ai}, \quad j = 2, 4, \dots, 2M,$$

$$b_j^{Ai} = b_{j+1}^{B(i-1)}, \quad j = 2, 4, \dots, 2M - 2, \quad (57)$$

$$b_j^{Ai} = b_{j-1}^{B(i-1)}, \quad j = 3, 5, \dots, 2M - 1,$$

for $i \geq 1$. In particular, from Eqs. (56) and (57), we can derive the following relationships:

$$b_1^{Ai} = b_{3+2M-2i}^{A(M+1)} \text{ and } b_{2M}^{Ai} = b_{2i-2}^{A(M+1)}, \quad (58)$$

for $i = 2, 3, \dots, M$. Eq. (58) inspires us to specially consider the stacked sequence A1, B1, A2, B2, ..., AM, BM, A(M + 1), that is, there are $2M + 1$ layers of AMO tessellations and M unit cells in the radial direction in each layer. In this case, if we assign values to the radial edge lengths in the layers A1 and A($M + 1$) (i.e., b_j^{Ai} and $b_j^{A(M+1)}$ for $j = 1, 2, \dots, 2M$), then the lengths of radial edges in other layers can be uniquely determined layer by layer from Eqs. (56)–(58) for $i = 2, 3, \dots, M$. Additionally, we can use the sine rules to obtain the relationships of the circumferential edges:

$$a_j^{Bi} = a_j^{Ai}, \quad 1 \leq i \leq M,$$

$$a_j^{Ai} = a_1^{B(i-1)} + (b_1^{B(i-1)} - b_1^{Ai}) \frac{\sin(\alpha - \beta)}{\sin \beta}, \quad 2 \leq i \leq M + 1. \quad (59)$$

Fig. 9(b) illustrates the deployment of an 11-layer stacked metamaterial, in which the geometry of the AMO tessellation in the bottom layer (i.e., layer A1) is given by the geometric parameters in the third row of Table 1, and the radial edge lengths of the AMO tessellation in the top layer (i.e., layer A6) are assigned to be the same as those in layer A1. The angular motion of the tessellations belongs to category e, determined by the sector angles $\alpha = 0.375\pi$, $\beta = 0.35\pi$, and the circumferential cell number $N = 40$. Therefore, the deployable stacked metamaterial is non-flat-deployable, and has a locking mechanism at the closed state. We can also choose specially-designed geometric parameters to build deployable metamaterials with desired shapes and angular deployment behaviors. For example, we fix the AMO tessellation in the top layer (i.e., layer A6) as in the second row of Table 1, and prescribe the radial edges of the AMO tessellation in the bottom layer (i.e., layer A1) to have a constant length, i.e., the tessellation in the bottom layer is set to be singly curved. Then we obtain a flat-deployable metamaterial with a flat bottom surface and a parabolic top surface, as shown in Fig. 10.

Finally, we note that there is no multi-layer metamaterial with alternative layers (ABABA...) of doubly curved AMO tessellations. A

brief proof can be given by supposing we have such alternative layers, i.e., $a_j^{Ai} = a_j^{A(i-1)}$, $a_j^{Bi} = a_j^{B(i-1)}$, $b_j^{Ai} = b_j^{A(i-1)}$, $b_j^{Bi} = b_j^{B(i-1)}$. Then we can obtain $b_j^{Ai} = b_{j+1}^{Ai}$ and $b_j^{Bi} = b_{j+1}^{Bi}$ from Eqs. (56)–(59), which leads to a contradictory result that the AMO tessellations are singly curved. The lack of alternatively stacked configurations reflect the discrepancy between doubly and singly curved AMO tessellations.

6. Conclusions

To conclude, we provide a systematic study on the deployment kinematics of axisymmetric Miura origami (AMO) at three hierarchical levels from unit cells to tessellations and stacked metamaterials. Firstly, we show that the AMO cells can exhibit monotonic and non-monotonic angular motion for different values of sector angles. Secondly, we demonstrate that diverse deploying behaviors will emerge if the AMO cells are tessellated to compose AMO tessellations. Depending on the circumferential cell number and the unit cell geometry, AMO tessellations can exhibit different deployment kinematics, characterized by the developability, flat-deployability, and closability. Thirdly, we generalize the kinematic formulations from singly curved to doubly curved AMO tessellations, the latter of which have non-uniform distributions of radial edge lengths, and therefore can form curved shapes in both circumferential and radial directions. Benefiting from the analytical formulations of the deployment kinematics, we develop an easy-to-implement optimization framework for the design of doubly curved AMO tessellations that approximate surfaces of revolution. Finally, we show that the deployability of stacked AMO metamaterials requires additional conditions for matching the angular motion of origami tessellations in adjacent layers. The stacking constraints for the singly curved and doubly curved tessellations are presented separately. The present study assumes that the thickness of the trapezoidal panels is zero, which lays the foundation for future work that incorporates a finite panel thickness for engineering applications.

CRediT authorship contribution statement

Xiangxin Dang: Conceptualization, Methodology, Software, Validation, Formal analysis, Investigation, Data curation, Writing – original draft, Writing – review & editing, Visualization. **Lu Lu:** Conceptualization, Methodology, Writing – review & editing, Resources, Funding acquisition. **Huiling Duan:** Conceptualization, Writing – review & editing, Resources, Supervision, Project administration, Funding acquisition. **Jianxiang Wang:** Conceptualization, Methodology, Validation, Writing – review & editing, Resources, Supervision, Project administration, Funding acquisition.

Declaration of competing interest

The authors declare that they have no known competing financial interests or personal relationships that could have appeared to influence the work reported in this paper.

Data availability

Data will be made available on request.

Acknowledgments

The authors thank the National Natural Science Foundation of China (Grants No. 11991033, and No. 91848201) for support of this work. L.L. thanks the China Postdoctoral Science Foundation (Grant No. 2020TQ0006) for support.

References

- [1] Amar MB, Müller MM, Trejo M. Petal shapes of sympetalous flowers: the interplay between growth, geometry and elasticity. *New J Phys* 2012;14(8):085014. <http://dx.doi.org/10.1088/1367-2630/14/8/085014>.
- [2] Carvajal D, Laprade EJ, Henderson KJ, Shull KR. Mechanics of pendant drops and axisymmetric membranes. *Soft Matter* 2011;7(22):10508–19. <http://dx.doi.org/10.1039/c1sm05703k>.
- [3] Faghah AK, Bahadori MN. Thermal performance evaluation of domed roofs. *Energy Build* 2011;43(6):1254–63. <http://dx.doi.org/10.1016/j.enbuild.2011.01.002>.
- [4] Nasir AM. Axisymmetric shell structures for multi-use (Ph.D. thesis), Queensland University of Technology; 2002.
- [5] Ghali A. Circular storage tanks and silos. CRC Press; 2014, <http://dx.doi.org/10.1201/b16887>.
- [6] Guest SD. Deployable structures: concepts and analysis (Ph.D. thesis), University of Cambridge; 1994.
- [7] Pellegrino S. Deployable structures. Springer; 2001, <http://dx.doi.org/10.1007/978-3-7091-2584-7>.
- [8] Adrover ER. Deployable structures. Laurence King Publishing; 2015.
- [9] Melancon D, Gorissen B, García-Mora CJ, Hoberman C, Bertoldi K. Multistable inflatable origami structures at the metre scale. *Nature* 2021;592(7855):545–50. <http://dx.doi.org/10.1038/s41586-021-03407-4>.
- [10] Ren Z, Hu W, Dong X, Sitti M. Multi-functional soft-bodied jellyfish-like swimming. *Nature Commun* 2019;10(1):1–12. <http://dx.doi.org/10.1038/s41467-019-10549-7>.
- [11] Jin D, Chen Q, Huang T-Y, Huang J, Zhang L, Duan H. Four-dimensional direct laser writing of reconfigurable compound micromachines. *Mater Today* 2020;32:19–25. <http://dx.doi.org/10.1016/j.mattod.2019.06.002>.
- [12] Kuribayashi K, Tsuchiya K, You Z, Tomus D, Umemoto M, Ito T, Sasaki M. Self-deployable origami stent grafts as a biomedical application of Ni-rich TiNi shape memory alloy foil. *Mater Sci Eng A* 2006;419(1):131–7. <http://dx.doi.org/10.1016/j.msea.2005.12.016>.
- [13] Beech R. Origami: the complete guide to the art of paperfolding. Lorenz Books; 2001.
- [14] Demaine ED, O'Rourke J. Geometric folding algorithms: linkages, origami, polyhedra. Cambridge University Press; 2007.
- [15] Lang RJ. Origami design secrets: mathematical methods for an ancient art. AK Peters/CRC Press; 2011.
- [16] Hull T. Project origami: activities for exploring mathematics. CRC Press; 2012.
- [17] Callens SJ, Zadpoor AA. From flat sheets to curved geometries: Origami and kirigami approaches. *Mater Today* 2018;21(3):241–64. <http://dx.doi.org/10.1016/j.mattod.2017.10.004>.
- [18] Huffman DA. Curvature and creases: A primer on paper. *IEEE Trans Comput* 1976;25(10):1010–9. <http://dx.doi.org/10.1109/TC.1976.1674542>.
- [19] Kawasaki T. On the relation between mountain-creases and valley-creases of a flat origami. In: Proceedings of the second international meeting of origami science and scientific origami; 1989.
- [20] Tachi T. Generalization of rigid-foldable quadrilateral-mesh origami. *J Int Assoc Shell Spat Struct* 2009;50(3):173–9.
- [21] Tachi T. Freeform variations of origami. *J Geom Graph* 2010;14(2):203–15.
- [22] Wu W, You Z. Modelling rigid origami with quaternions and dual quaternions. *Proc R Soc Lond Ser A Math Phys Eng Sci* 2010;466(2119):2155–74. <http://dx.doi.org/10.1098/rspa.2009.0625>.
- [23] Gattas JM, Wu W, You Z. Miura-base rigid origami: Parameterizations of first-level derivative and piecewise geometries. *J Mech Des* 2013;135(11):111011. <http://dx.doi.org/10.1115/1.4025380>.
- [24] Chen Y, Peng R, You Z. Origami of thick panels. *Science* 2015;349(6246):396–400. <http://dx.doi.org/10.1126/science.aab2870>.
- [25] Sareh P, Guest S. Design of isomorphic symmetric descendants of the miura-ori. *Smart Mater Struct* 2015;24:085001. <http://dx.doi.org/10.1088/0964-1726/24/8/085001>.
- [26] Sareh P, Guest S. Design of non-isomorphic symmetric descendants of the miura-ori. *Smart Mater Struct* 2015;24:085002. <http://dx.doi.org/10.1088/0964-1726/24/8/085002>.
- [27] Zhou X, Wang H, You Z. Design of three-dimensional origami structures based on a vertex approach. *Proc R Soc Lond Ser A Math Phys Eng Sci* 2015;471:20150407. <http://dx.doi.org/10.1098/rspa.2015.0407>.
- [28] Abel Z, Cantarella J, Demaine ED, Eppstein D, Hull TC, Ku JS, Lang RJ, Tachi T. Rigid origami vertices: Conditions and forcing sets. *J Comput Geom* 2016;7(1):171–84.
- [29] Cai J, Zhang Y, Xu Y, Zhou Y, Feng J. The foldability of cylindrical foldable structures based on rigid origami. *J Mech Des* 2016;138(3). <http://dx.doi.org/10.1115/1.4032194>.
- [30] Demaine ED, Tachi T. Origamizer: A practical algorithm for folding any polyhedron. In: Aronov B, Katz MJ, editors. 33rd international symposium on computational geometry (SoCG 2017). Leibniz international proceedings in informatics (LIPIcs), vol. 77, Schloss Dagstuhl–Leibniz-Zentrum fuer Informatik; 2017, p. 34:1–16. <http://dx.doi.org/10.4230/LIPIcs.SoCG.2017.34>.
- [31] Lang RJ, Howell L. Rigidly foldable quadrilateral meshes from angle arrays. *J Mech Robot* 2018;10(2):021004. <http://dx.doi.org/10.1115/1.4038972>.
- [32] Dieleman P, Vasmel N, Waitukaitis S, van Hecke M. Jigsaw puzzle design of pluripotent origami. *Nat Phys* 2020;16(1):63–8. <http://dx.doi.org/10.1038/s41567-019-0677-3>.
- [33] Feng F, Dang X, James RD, Plucinsky P. The designs and deformations of rigidly and flat-foldable quadrilateral mesh origami. *J Mech Phys Solids* 2020;142:104018. <http://dx.doi.org/10.1016/j.jmps.2020.104018>.
- [34] McInerney J, Chen BG-g, Theran L, Santangelo CD, Rocklin DZ. Hidden symmetries generate rigid folding mechanisms in periodic origami. *Proc Natl Acad Sci USA* 2020;117(48):30252–9. <http://dx.doi.org/10.1073/pnas.2005089117>.
- [35] Dudte LH, Choi GPT, Mahadevan L. An additive algorithm for origami design. *Proc Natl Acad Sci USA* 2021;118(21):e2019241118. <http://dx.doi.org/10.1073/pnas.2019241118>.
- [36] Fonseca LM, Rodrigues GV, Savi MA. An overview of the mechanical description of origami-inspired systems and structures. *Int J Mech Sci* 2022;223:107316. <http://dx.doi.org/10.1016/j.ijmecsci.2022.107316>.
- [37] Miura K. Method of packaging and deployment of large membranes in space. *Inst Space Astronaut Sci Rep* 1985;618:1–9.
- [38] Zirbel SA, Lang RJ, Thomson MW, Sigel DA, Walkemeyer PE, Trease BP, Magleby SP, Howell LL. Accommodating thickness in origami-based deployable arrays. *J Mech Des* 2013;135(11):111005. <http://dx.doi.org/10.1115/1.4025372>.
- [39] Filipov ET, Tachi T, Paulino GH. Origami tubes assembled into stiff, yet reconfigurable structures and metamaterials. *Proc Natl Acad Sci USA* 2015;112(40):12321–6. <http://dx.doi.org/10.1073/pnas.1509465112>.
- [40] Li Y, Chandra A, Dorn CJ, Lang RJ. Reconfigurable surfaces employing linear-rotational and bistable-translational (LRBT) joints. *Int J Solids Struct* 2020;207:22–41. <http://dx.doi.org/10.1016/j.ijsolstr.2020.09.029>.
- [41] Felton S, Tolley M, Demaine E, Rus D, Wood R. A method for building self-folding machines. *Science* 2014;345(6197):644–6. <http://dx.doi.org/10.1126/science.1252610>.
- [42] Rus D, Tolley MT. Design, fabrication and control of origami robots. *Nat Rev Mater* 2018;3(6):101–12. <http://dx.doi.org/10.1038/s41578-018-0009-8>.
- [43] Kim W, Byun J, Kim J-K, Choi W-Y, Jakobsen K, Jakobsen J, Lee D-Y, Cho K-J. Bioinspired dual-morphing stretchable origami. *Sci Robot* 2019;4(36):eaay3493. <http://dx.doi.org/10.1126/scirobotics.aay3493>.
- [44] Dudte LH, Vouga E, Tachi T, Mahadevan L. Programming curvature using origami tessellations. *Nature Mater* 2016;15(5):583–8. <http://dx.doi.org/10.1038/nmat4540>.
- [45] Wang F, Gong H, Chen X, Chen C. Folding to curved surfaces: A generalized design method and mechanics of origami-based cylindrical structures. *Sci Rep* 2016;6:33312. <http://dx.doi.org/10.1038/srep33312>.
- [46] Song K, Zhou X, Zang S, Wang H, You Z. Design of rigid-foldable doubly curved origami tessellations based on trapezoidal crease patterns. *Proc R Soc Lond Ser A Math Phys Eng Sci* 2017;473:20170016. <http://dx.doi.org/10.1098/rspa.2017.0016>.
- [47] Hu Y, Liang H, Duan H. Design of cylindrical and axisymmetric origami structures based on generalized miura-ori cell. *J Mech Robot* 2019;11(5):051004. <http://dx.doi.org/10.1115/1.4043800>.
- [48] Hu Y, Zhou Y, Liang H. Constructing rigid-foldable generalized miura-ori tessellations for curved surfaces. *J Mech Robot* 2021;13(1):011017. <http://dx.doi.org/10.1115/1.4048630>.
- [49] Dang X, Feng F, Plucinsky P, James RD, Duan H, Wang J. Inverse design of deployable origami structures that approximate a general surface. *Int J Solids Struct* 2022;234:111224. <http://dx.doi.org/10.1016/j.ijsolstr.2021.111224>.
- [50] Rogers J, Huang Y, Schmidt OG, Gracias DH. Origami MEMS and NEMS. *Mrs Bull* 2016;41(2):123–9. <http://dx.doi.org/10.1557/mrs.2016.22>.
- [51] Schenk M, Guest SD. Geometry of miura-folded metamaterials. *Proc Natl Acad Sci USA* 2013;110(9):3276–81. <http://dx.doi.org/10.1073/pnas.1217998110>.
- [52] Wei ZY, Guo ZV, Dudte L, Liang HY, Mahadevan L. Geometric mechanics of periodic pleated origami. *Phys Rev Lett* 2013;110(21):215501. <http://dx.doi.org/10.1103/PhysRevLett.110.215501>.
- [53] Zhao S, Zhang Y, Zhang Y, Yang J, Kitipornchai S. Graphene origami-enabled auxetic metallic metamaterials: An atomistic insight. *Int J Mech Sci* 2021;212:106814. <http://dx.doi.org/10.1016/j.ijmecsci.2021.106814>.
- [54] Ma J, Song J, Chen Y. An origami-inspired structure with graded stiffness. *Int J Mech Sci* 2018;136:134–42. <http://dx.doi.org/10.1016/j.ijmecsci.2017.12.026>.
- [55] Yuan L, Dai H, Song J, Ma J, Chen Y. The behavior of a functionally graded origami structure subjected to quasi-static compression. *Mater Des* 2020;189:108494. <http://dx.doi.org/10.1016/j.matdes.2020.108494>.
- [56] Waitukaitis S, Menaut R, Chen BG-g, Van Hecke M. Origami multistability: From single vertices to metasheets. *Phys Rev Lett* 2015;114(5):055503. <http://dx.doi.org/10.1103/PhysRevLett.114.055503>.

- [57] Liu K, Tachi T, Paulino GH. Invariant and smooth limit of discrete geometry folded from bistable origami leading to multistable metasurfaces. *Nature Commun* 2019;10(1):1–10. <http://dx.doi.org/10.1038/s41467-019-11935-x>.
- [58] Feng F, Plucinsky P, James RD. Helical miura origami. *Phys Rev E* 2020;101:033002. <http://dx.doi.org/10.1103/PhysRevE.101.033002>.
- [59] Li Y, Pellegrino S. A theory for the design of multi-stable morphing structures. *J Mech Phys Solids* 2020;136:103772. <http://dx.doi.org/10.1016/j.jmps.2019.103772>.
- [60] Xiang X, Lu G, You Z. Energy absorption of origami inspired structures and materials. *Thin-Walled Struct* 2020;157:107130. <http://dx.doi.org/10.1016/j.tws.2020.107130>.
- [61] Xu J, Fu C, Fu Q, Chen Y, Ma Y, Feng X. Flexible arc-armor inspired by origami. *Int J Mech Sci* 2021;201:106463. <http://dx.doi.org/10.1016/j.ijmecsci.2021.106463>.
- [62] Silverberg JL, Evans AA, McLeod L, Hayward RC, Hull T, Santangelo CD, Cohen I. Using origami design principles to fold reprogrammable mechanical metamaterials. *Science* 2014;345(6197):647–50. <http://dx.doi.org/10.1126/science.1252876>.
- [63] Reid A, Lechenault F, Rica S, Adda-Bedia M. Geometry and design of origami bellows with tunable response. *Phys Rev E* 2017;95:013002. <http://dx.doi.org/10.1103/PhysRevE.95.013002>.
- [64] Fang H, Li S, Ji H, Wang KW. Uncovering the deformation mechanisms of origami metamaterials by introducing generic degree-four vertices. *Phys Rev E* 2016;94:043002. <http://dx.doi.org/10.1103/PhysRevE.94.043002>.
- [65] Fang H, Chu S-CA, Xia Y, Wang K-W. Programmable self-locking origami mechanical metamaterials. *Adv Mater* 2018;30(15):1706311. <http://dx.doi.org/10.1002/adma.201706311>.
- [66] Zhai Z, Wang Y, Jiang H. Origami-inspired, on-demand deployable and collapsible mechanical metamaterials with tunable stiffness. *Proc Natl Acad Sci USA* 2018;115(9):2032–7. <http://dx.doi.org/10.1073/pnas.1720171115>.
- [67] Pratapa PP, Liu K, Paulino GH. Geometric mechanics of origami patterns exhibiting Poisson's ratio switch by breaking mountain and valley assignment. *Phys Rev Lett* 2019;122(15):155501. <http://dx.doi.org/10.1103/PhysRevLett.122.155501>.
- [68] He Y, Zhang P, You Z, Li Z, Wang Z, Shu X. Programming mechanical metamaterials using origami tessellations. *Compos Sci Technol* 2020;189:108015. <http://dx.doi.org/10.1016/j.compscitech.2020.108015>.
- [69] Lyu S, Qin B, Deng H, Ding X. Origami-based cellular mechanical metamaterials with tunable Poisson's ratio: Construction and analysis. *Int J Mech Sci* 2021;212:106791. <http://dx.doi.org/10.1016/j.ijmecsci.2021.106791>.
- [70] Kresling B, Abel JF, Cooke R. Natural twist buckling in shells: from the hawkmoth's bellows to the deployable Kresling-pattern and cylindrical Miuraori. In: Proceedings of the 6th international conference on computation of shell and spatial structures, Vol. 11; 2008, p. 12–32.
- [71] Silverberg JL, Na J-H, Evans AA, Liu B, Hull TC, Santangelo CD, Lang RJ, Hayward RC, Cohen I. Origami structures with a critical transition to bistability arising from hidden degrees of freedom. *Nature Mater* 2015;14(4):389–93. <http://dx.doi.org/10.1038/nmat4232>.
- [72] Resch RD. The topological design of sculptural and architectural systems. In: Proceedings of the June 4–8, 1973, national computer conference and exposition. AFIPS '73, New York, NY, USA: Association for Computing Machinery; 1973, p. 643–50. <http://dx.doi.org/10.1145/1499586.1499744>.
- [73] Chen Y, Feng H, Ma J, Peng R, You Z. Symmetric waterbomb origami. *Proc R Soc Lond Ser A Math Phys Eng Sci* 2016;472(2190):20150846. <http://dx.doi.org/10.1098/rspa.2015.0846>.